Paper ID: 486

Measurements of xenon ions and atoms velocity in Cylindrical Hall Thruster with Laser-Induced Fluorescence spectroscopy

Tatiana Perrotin[*][†], *Stéphane Mazouffre*[‡], *Alfio E. Vinci*[‡][#], *Eduardo Ahedo*[*], *Pablo Fajardo*[*] *and Jaume Navarro-Cavallé*[*]
[*]*Equipo de Populsión Espacial y Plasmas (EP2), Universidad Carlos III de Madrid*
Avenida de la Universidad, 30, 28911 Leganés, Spain
[‡]*Institut de Combustion, Aérothermique, Réactivité et Environnement (ICARE), CNRS*
1C avenue de la Recherche Scientifique, 45071 Orléans, France
tperroti@pa.uc3m.es · stephane.mazouffre@cnrs-orleans.fr · alfio.emanuele.vinci@thrustme.fr · eahedo@ing.uc3m.es
pfajardo@ing.uc3m.es · janavarr@ing.uc3m.es
[†]Corresponding author, [#]Institution of the author at the time of the contribution

Abstract

The Velocity Distribution Function of the xenon ions and atoms was measured by means of Laser-Induced Fluorescence spectroscopy in a plasma thruster. The device characterized was a miniaturized Cylindrical Hall Thruster designed to operate in the discharge power range of 100 - 300 W. The axial component of the velocity was probed at multiple axial and radial positions inside the discharge chamber and in the near-field. The results allowed for identifying the ionization and acceleration regions, estimating the axial electric field, and observing the effects of the peculiar magnetic topology of the CHT on the ions. The experimental fluorescence lineshapes were reconstructed using a theoretical model to distinguish the features of the VDF from any broadening mechanisms that modify the aspect of the optical transition.

1. Introduction

The development of low-power electric thrusters is motivated by the growing interest in using these devices onboard small satellites, such as the ones used for Low-Earth Orbit constellations, in order to have the ability to perform some orbit maneuvers, such as orbit raising, small transfers at injection, or de-orbiting, for instance. The Hall Effect Thruster (HET) is a mature technology that offers high thrust and efficiency compared to most other options. A major asset of HETs is their throttability while they require reasonably simple electronics. However, scaling them to low-power is challenging, and both the lifetime and the performance are altered.

Small-sized HETs present increased power losses to the walls due to the large surface-to-volume ratio. This issue can be mitigated by using a cylindrical discharge chamber instead of the traditional annular one. Reducing the length of the central pole also somewhat simplifies the machining and thermal management of some thruster parts.[1] However, such a change in geometry brings important alterations to the magnetic topology, which is no longer purely radial. This has an impact on the shape of the electric field and the particle fluxes to the walls.

Due to the peculiar magnetic topology in the discharge chamber, questions arise regarding the location of the ionization and acceleration regions, and whether the design can be optimized by better identifying them. Acquiring information on the behavior of the plasma species inside the channel is difficult given the small room available and the risk of perturbing the plasma discharge both locally and globally. The use of simple electrostatic probes is thus nearly impossible to obtain reliable data. For that reason, optical diagnostics are employed since they are non-intrusive and offer a sufficiently high spatial resolution for the characteristic dimensions of this type of thruster. Laser-Induced Fluorescence (LIF) spectroscopy is a sensitive and accurate optical diagnostic that allows for measuring the Velocity Distribution Function (VDF) of heavy species such as atoms, ions, or molecules, selectively. Other magnitudes can be derived from the measurements, such as the particle temperature, density, and ambient electric and magnetic fields.[2,3]

While LIF spectroscopy has already been used in various types of plasma thrusters[4–6] including annular HETs,[3,7–9] few measurements in the plasma discharge of a Cylindrical Hall Thruster (CHT) can be found in literature.[10–12] The available data mainly focuses on the region near the thruster exit plane and provides information on the ion velocity vector, with measurements in the axial and radial directions.

Low-power Hall Thrusters, specifically fully cylindrical ones, are characterized by the presence of a strong applied magnetic field that can reach 1 to 2 kG near the central pole to ensure electron confinement and anode shielding. This strong magnetic field is one of the multiple factors that can modify the fluorescence signal, consequently, the LIF spectra
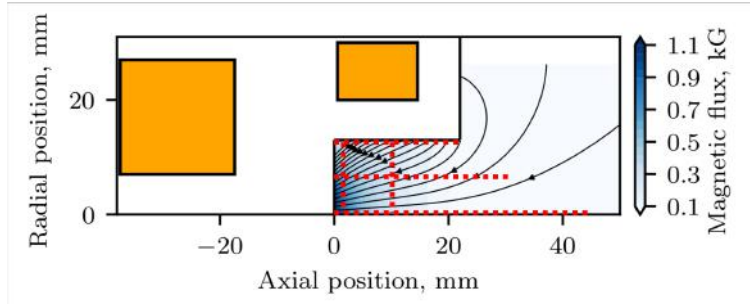
Figure 1: Magnetic flux and streamlines of the CHT, with probed locations (red).
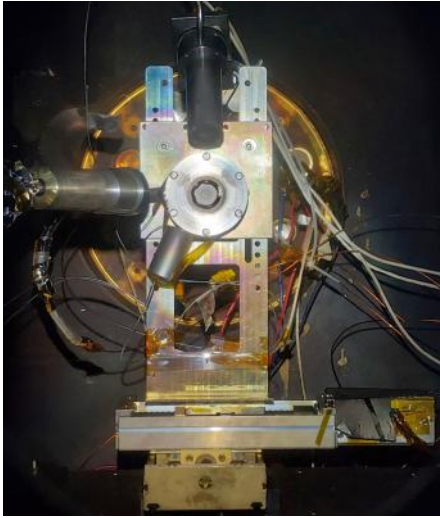

Figure 2: Experimental setup on the vacuum side, with the detection lens (left), and axial and radial translation stages (bottom) on which the thruster (center) and cathode (top) are mounted.
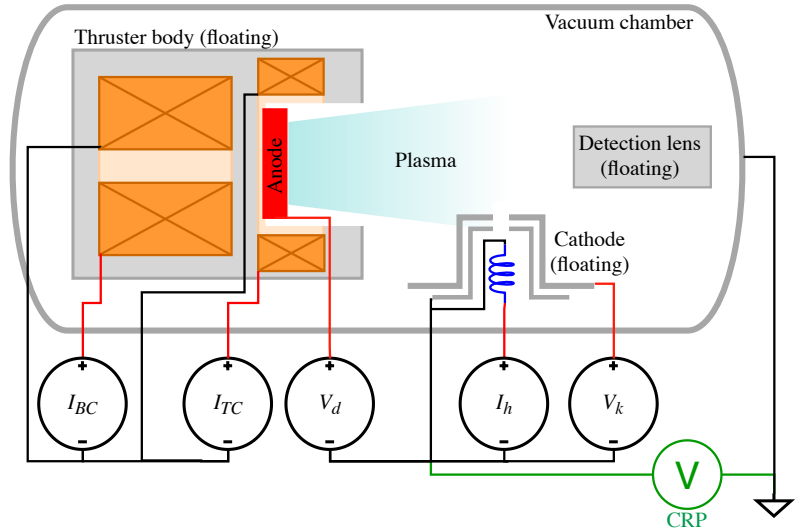
Figure 3: Schematic of the electrical setup.

no longer represent the particle VDF in a straightforward way. In such a case, it becomes necessary to retrieve the real VDF by using theoretical models.[13]

The present work intends to provide LIF spectra measurements of the axial VDF of xenon ions, inside the discharge chamber and in the near-field of a 200 W fully Cylindrical Hall Thruster. Measurements of the xenon atoms VDF in the vicinity of the gas injector are provided, and lineshape reconstruction using a theoretical model is performed to better analyze the experimental results. The neutral VDF measurement and spectra simulations are novelties in CHT to the knowledge of the authors.

The thruster and cathode tested are described in Section 2 along with the test facility. The LIF bench is introduced as well, after a brief presentation of the underlying physical principles. The results of the ion and neutral velocity measurements are given in Section 3 and 4, respectively. Section 5 provides a short explanation of the principle of the lineshape model used in this work and some results are shown, before drawing general conclusions in Section 6.

2. Experimental setup

2.1 Thruster and cathode

The thruster used in this work is a CHT designed to operate around 100 - 300 W of discharge power. It is made of a 22 mm-long, 13 mm-radius cylindrical boron nitride channel similar to the one designed by Raitses.[14,15] It does not have any coaxial region, thus the upstream wall of the discharge chamber ends flush with the annular copper anode. The latter possesses six holes for propellant injection that are evenly distributed in the azimuthal direction in order to optimize

ionization and plume symmetry.[16] Figure 1 shows the magnetic field $\vec{B}$ that is generated by two coils powered in direct configuration, with 1 A and 1.7 A of current in the downstream and upstream coils, respectively. The direct field is meant to limit the beam divergence and large electron flux to the wall that can be observed with a cusped field.[17, 18] The field is shaped by the soft iron components of the thruster, which are the casing and an internal central pole placed in the upstream coil and covered by the ceramic back wall of the channel. A more detailed description of the thruster is available in previous works.[19, 20]

The thruster was paired with a MIREA-type thermionic cathode made of a LaB_6 pellet-shaped emitter.[21] It was positioned in such a way that the keeper orifice was 55 mm away from the thruster axis, vertically, and 30 mm downstream the exit plane, with the cathode axis oriented at 45 ° with respect to the thruster axis (Fig. 2). Since this neutralizer is sized to deliver 5 A of current, the anode discharge current was insufficient for it to be self-heated. As a consequence, some power was supplied to the heater during thruster operation and a keeper current of 2.5 A was maintained while testing. The heating power was tuned between 100 and 250 W along the measurements to get similar discharge conditions and keep a Cathode Reference Potential (CRP) around -16 ±3 V. The CRP is defined as the potential difference between the grounded vacuum chamber and the cathode (Fig. 3). The mass flow rates of high-purity xenon fed to the anode and the cathode were set independently with two Alicat MC-series Mass Gas Flow Controllers, calibrated for this propellant. All the tests were performed with a cathode flow rate of 2 sccm. The main discharge was always controlled in voltage. Both the thruster-casing and the cathode are electrically floating with respect to the vacuum chamber and to one another (Fig. 3).

The data presented in this paper were acquired under discharge conditions maintained as constant as possible with a discharge voltage V_d = 300 V, an anode current $I_a \approx 0.5$ A, an anode xenon mass flow rate $\dot{m}_a$ = 3.8 sccm, a cathode xenon mass flow rate $\dot{m}_c$ = 2 sccm, a keeper current I_k = 2.5 A, a CRP $\approx$ -16 V and a cathode heater power P_h varied freely from 104 to 260 W. However, note that spontaneous evolution of the thruster operation occurred and was observed on the average value of discharge current, and on its frequency spectrum. This also caused the acceleration region to slightly drift downstream for the quarter-line measurements, in comparison to the previously done axis measurements. To counteract those natural variations, the anode mass flow had to be adjusted and thus the ion velocity measurements on the axis were taken with $\dot{m}_a$ = 3.5 sccm to maintain a similar discharge current over the whole test. The cathode heater power was continuously adapted over the test campaign.

2.2 Test facility

The experiments presented hereafter were performed in the New Experiment on Electric Thrusters (NExET) vacuum chamber, which consists of a 1.8 m-long, 0.8 m-diameter stainless steel cylindrical vessel. The facility is equipped with a primary pump, a turbomolecular pump, and a cryogenic panel cooled down to approximately 40 K. This allows for reaching a base pressure in the order of 10^{-7} mbar. During the tests, the chamber pressure was maintained below 3×10^{-5} mbar with a total xenon mass flow rate under 6 sccm. The vacuum chamber was grounded electrically, and the structure supporting the thruster, cathode, and detection lens, was kept electrically floating (Fig. 3). The thruster and cathode assembly was mounted on two translation stages (Fig. 2) allowing displacement in the axial and radial directions. The temperature of the downstream electromagnet of the thruster was monitored using a K-type thermocouple.

2.3 LIF spectroscopy

2.3.1   Physical principle

LIF spectroscopy is a diagnostic technique that allows for measuring various properties of a selected species, such as the velocity, temperature, and density, without disturbing the plasma by inserting probes in the volume of interest. The process relies on bringing a target population from one quantum level to another one of higher energy, by absorption of a photon of energy $E = h\nu$ that matches the difference between the two levels.[2, 3] After the probed ion or atom is excited with the laser, it naturally deexcites to a lower energy state by emitting a photon, this spontaneous phenomenon is called fluorescence and is isotropic. For a given particle, the energies allowed for these two optical transitions are bound by selection rules. In the case of moving particles, the absorption frequency is shifted due to the Doppler effect, according to:

$$\Delta\nu = \nu - \nu_0 = \frac{\mathbf{k} \cdot \mathbf{v}}{2\pi}. \tag{1}$$

where $\mathbf{v}$ is the particle velocity vector, $\mathbf{k}$ is the laser wave vector and ν is the laser wave frequency. The sign of the shift depends on the direction of motion with respect to the laser wave vector. The VDF can thus be retrieved by performing a sweep of the laser frequency, since the particles with different velocities have a different shift, and the
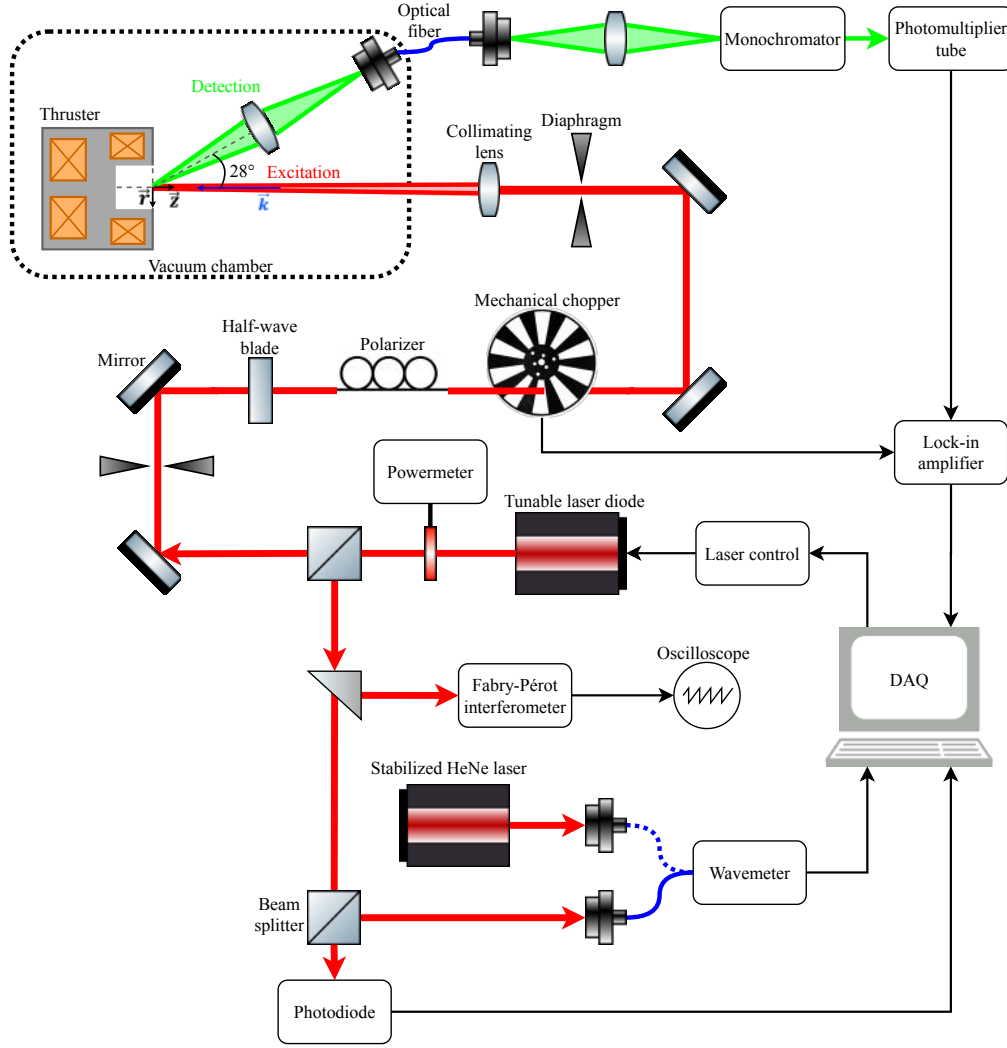
Figure 4: Schematic of the LIF test bench and vacuum-side optical setup.

fluorescence signal intensity is proportional to the density of the particles emitting. In practice, the measured LIF lineshape corresponds to the convolution of the multiple broadening or splitting mechanisms such as the initial laser spectrum, natural linewidth, hyperfine structure, isotopic shifts, Stark effect due to an external electric field, Zeeman effect due to an external magnetic field, with a dependence on the polarization of the beam, and the particle VDF.[22, 23] These mechanisms all introduce additional allowed transitions, thus making the lineshape very distorted compared to an ideal theoretical Dirac.

In the figures presented hereafter in Sections 3 and 4, the lineshapes are given as a function of the velocity rather than the wavelength in order to ease the reading, with:

$$v = c\left(\frac{\lambda_0 - \lambda}{\lambda_0}\right) \tag{2}$$

where v is the velocity in the probed direction, c is the speed of light in vacuum, λ is the wavelength and λ_0 is the wavelength of the optical transition for a non-moving particle.

2.3.2 Optical bench

The LIF bench used for the measurements is represented in Fig. 4. The excitation branch (red) contains an amplified tunable single-mode laser diode used for the optical pumping of the probed population. The beam goes through a half-wave blade and a polarizer to ensure that it is polarized linearly, orthogonally to the thruster magnetic field in the plane of measurement, and then through a mechanical chopper with a modulation frequency of 521 Hz. The laser

Table 1: Xenon atoms and ions probed transitions

Species		Transition	Wavelength in air (nm)
Xe I	Excitation	$5p^5(^2P^\circ_{1/2})6s^2[1/2]^\circ_1 \rightarrow 5p^5(^2P^\circ_{1/2})6p^2[3/2]_2$	834.68217
	Fluorescence	$5p^5(^2P^\circ_{1/2})6p^2[3/2]_2 \rightarrow 5p^5(^2P^\circ_{3/2})6s^2[3/2]^\circ_1$	473.41
Xe II	Excitation	$5s^25p^4(^3P_2)5d^2[4]_{7/2} \rightarrow 5s^25p^4(^3P_2)6p^2[3]^\circ$	834.724
	Fluorescence	$5s^25p^4(^3P_2)6p^2[3]^\circ \rightarrow 5s^25p^4(^3P_2)6s^2[2]_{3/2}$	541.91

beam is collimated with a lens of focal length F = 140 cm and injected directly inside the vacuum chamber through a viewport.

A powermeter is used to systematically ensure that the laser power density is around 2 mW.mm^{-2} in the probed region, and avoid saturation effects. The appropriate power density to use was determined experimentally.[7] The beam is split to be analyzed by various instruments. A Fabry-Perot interferometer and an oscilloscope allow for tracking mode-hops and laser mode quality. A photodiode is used to measure the laser beam intensity during the scans, and the wavelength is accurately measured using a wavemeter regularly calibrated with a stabilized HeNe laser at 632.9914 nm.

The detection branch is composed of a lens of focal distance F = 60 mm, positioned in the measurement plane with an angle of 28 ° with respect to the thruster axis. This lens collects and focuses the fluorescence light into an optical fiber which carries it from the vacuum side to the air side. The signal passes through another lens and is fed to a monochromator tuned to the fluorescence wavelength to isolate the selected line. A photomultiplier then converts the light into an electric signal which is provided to a lock-in amplifier that is itself synchronized to the chopper frequency in order to separate this light from the natural plasma emission. More detailed information about the LIF bench can be found in references.[5,7,13,22]

The laser and its amplifier are set manually to the desired parameters for a measurement, then, a wavelength sweep is performed via software that gathers the measured signal from the lock-in amplifier, the wavemeter information, and the laser intensity.

Probing various spatial locations is achieved by displacing the thruster and cathode in the axial and radial directions with two linear translation stages (Fig. 2). The probed locations are represented in Fig. 1 with dashed red lines. Given the magnetic topology of the thruster and the consequent diagonal effects on the plasma, scans are performed along the thruster axial direction at three radii ($r = 0$ mm, $r = 6.5$ mm and $r = 13$ mm) corresponding to the axis, the quarter-line, and the side wall. Ion behavior in the vicinity of the walls is of particular interest to characterize plasma-wall interaction and potentially improve the design. Scans along the radial directions are also performed, at $z = -14$ mm for the ions and $z = -20$ mm for the neutrals, with the reference $z = 0$ mm corresponding to the thruster exit plane.

The probed transitions are summarized in Table 1. The neutrals are probed in a resonant state and the ions in a metastable state, both selected to be sufficiently populated given the lifetime of their upper state while having an excitation wavelength accessible to the laser.

3. Metastable ions axial velocity

3.1 Axial evolution of lineshape

The setup used in this work allowed for measuring the axial component of the velocity. The evolution of the ion VDF along the axial direction is of particular interest to identify the location of the acceleration region, which is located downstream of the exit plan in traditional Hall thrusters. Figure 5 shows the evolution of the metastable ion VDF along the axial direction, on the thruster axis (top), quarter-line (middle), and side wall (bottom). The thruster channel upstream and downstream boundaries are indicated for reference. The plotted magnitude is the normalized raw lineshape, although to simplify the reading, the wavelength is converted to velocity with Eq. (2).

Figure 5 shows that the acceleration region starts more upstream on the axis and more downstream at larger radii. Particularly, the quarter-line displays an almost flat region on the left-hand side of the graph (upstream end of the plasma chamber) that shows very little acceleration, while on the axis, the ion velocity clearly increases even very close to the back wall.

Despite the limited scanned points in the exit plane region at the largest radius, one can see in Fig. 5 that the most probable ion axial velocity achieved around the exit plane is the same at all radii (≈ 15 km.s^{-1}). The final velocity is reached at 22 mm downstream the exit plane on the axis, and it is about 18.3 km.s^{-1}, while the maximum possible velocity given $V_d = 300$ V and CRP = -16 V is $v_{max} \approx 20.4$ km.s^{-1}. This is rather promising in terms of voltage utilization and could mean that losses in the ion acceleration do not come from a different axial potential drop seen by
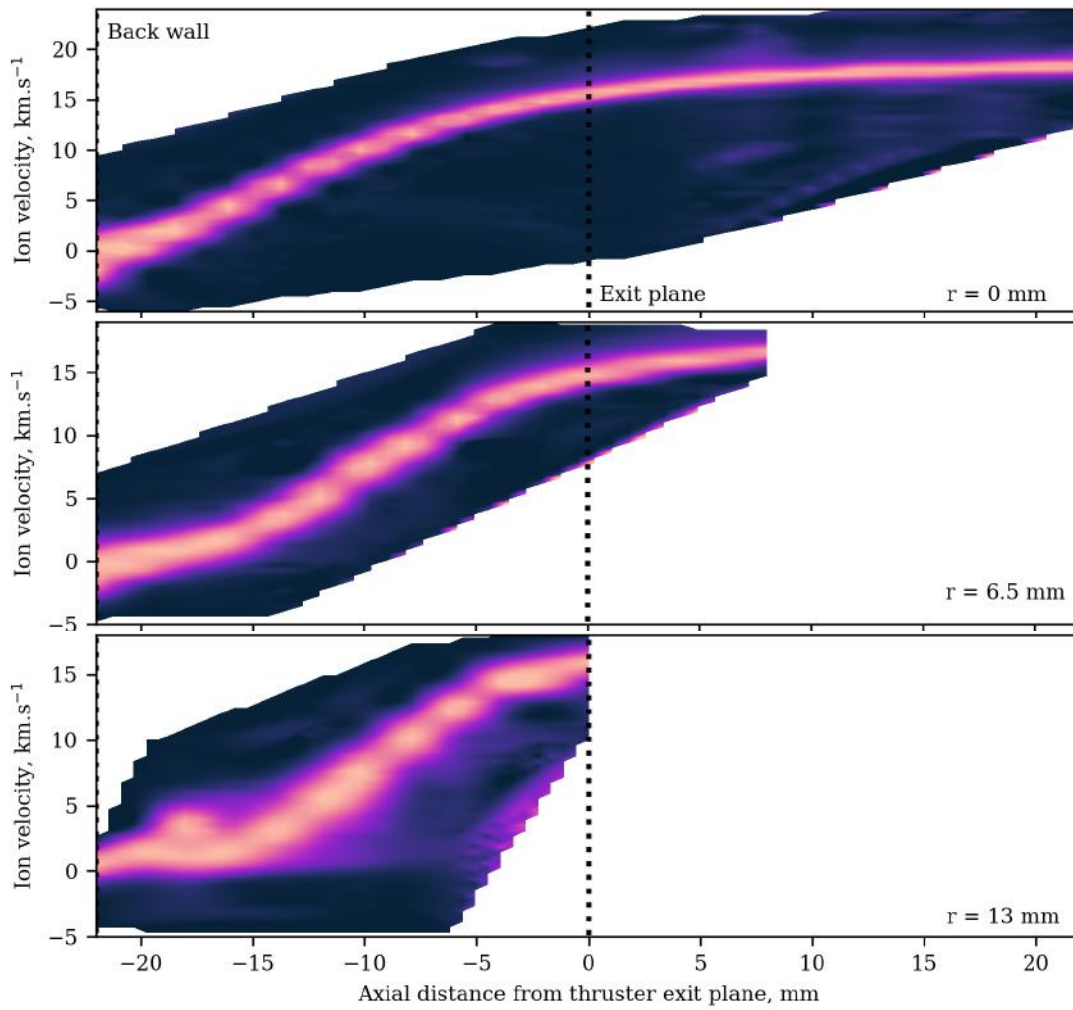
Figure 5: Evolution of the ion transition lineshape along the axial direction at three different radii.
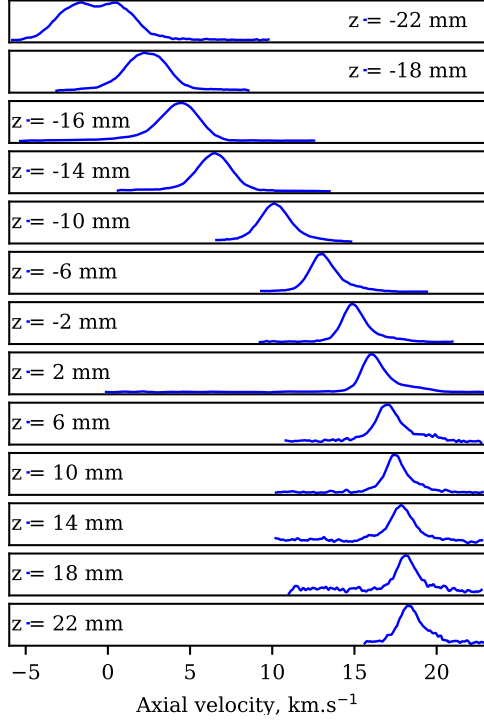
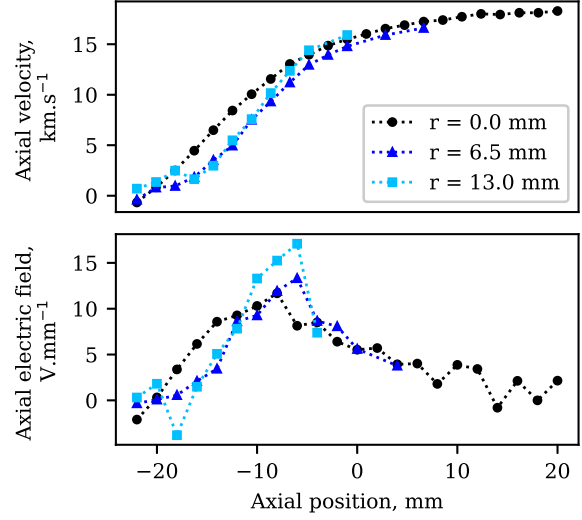Figure 6: Evolution of the ion transition lineshape along the thruster axis.

Figure 7: Evolution of the most probable ion axial velocity (top) and of the axial electric field (bottom), along the axial direction, at three radii.

the ions and introduced by the peculiar $\vec{B}$ topology. Yet, measurements at large radii in the plume, and knowledge of the radial velocity component would help clarify this and previous far-field velocity measurements.[20]

The bottom plot of Fig. 5 shows an accelerating main group of ions along with a secondary one that contains ions at all the velocities from 0 up to the velocity of the main group. This could indicate that the ionization region is very wide in the axial direction near the side wall, which is consistent with the magnetic topology. It could also be characteristic of the occurrence of ion recombination and re-ionization at the wall.

Some lineshapes of the ion transition on the axis, presented already in Fig. 5 (top), are given in Fig. 6 as a reference, to better highlight some features. At $z = -22$ mm, a negative ion velocity is measured which means that ions travel towards the back wall. Even though it is in the order of a few hundred meters per second, it appears to generate significant erosion of the ceramic since it got entirely perforated at the central pole after ≈ 200 hours of firing. In addition, at the same axial location, one can observe two peaks due to Zeeman broadening and splitting. Indeed, the magnetic field is very high in this region, about 975 G. Note that when probing very close to the wall, some weak part of the collected signal could come from the fluorescence of ions excited by the reflection of the laser in the ceramic, thus with an opposite Doppler shift. However, this does not appear to alter the lineshape in this case.

Around $z = -16$ mm, a slightly more populated tail of slow ions is visible and is attributed to the overlap between the ionization and acceleration regions. Ions created further downstream than the main group see a lower potential drop and have slower velocities. A complete scan of the full positive velocity range was performed at $z = 2$ mm and shows that there is no isolated slow ion population, which is sometimes observed in annular[24] and cylindrical HETs.[25] From $z \approx 6$ mm forward, the most probable velocity increases very little, so the acceleration region is almost entirely located inside the thruster chamber, and ions are fully accelerated a few millimeters downstream of the exit plane. A more populated tail of fast ions is visible at $z = 22$ mm and possibly results from ions created where the electric field is the largest, or from discharge oscillations allowing the electric field to take larger values for short periods of time, thus accelerating ions to larger velocities than the most probable one. The disappearance of the slow ion tail instead could be due to the fact that slow ions are accelerated with an angle and fewer are visible as z increases, which would be in agreement with previous observation in this thruster.[20] Locations further than 22 mm in the plume were not probed since the fluorescence signal was very low, noisy, and required an unreasonably long integration time.

Knowing the spatial variation of the axial velocity, the axial component of the electric field E_z is retrieved using the energy conservation,[3] with:

$$E_z = \frac{dV}{dz} = v\frac{m_i}{q}\frac{dv_{mp}}{dz}.$$
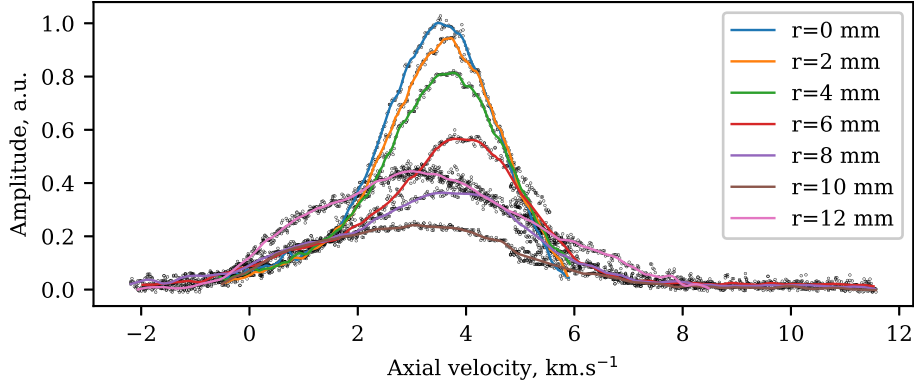
(3)

7

Figure 8: Evolution of the ion transition lineshape along the radial direction, at z = -14 mm, for seven radial locations. The axial component of the velocity is probed. The grey circles represent the raw lineshape and the solid lines show the smoothed data.

The evolution with z of the most probable velocity and of the axial electric field is given in Fig. 7 for all three radii scanned. As previously observed with Fig. 5, even though the velocity evolves differently depending on the radial location, the most probably velocity reaches approximately the same value at all radii when approaching the exit plane. The axial component of $\vec{E}$ is larger close to the wall than on the axis and quarter-line, although this is probably because the direction of the field is more axial close to the wall and partly radial at the quarter-line. On the axis, given the expected axisymmetry, the field should not have any radial component, and thus E_z should be representative of E. Surprisingly, E_z reaches its maximum at the same axial position for all radii, which is not the expected behavior in a CHT, if the magnetic streamlines are considered as almost isopotential lines.[19] This could indicate some interesting behavior in terms of cross-field electron transport but investigating it further would require diagnostics that allow for probing the electron dynamics.

Note that the apparent slowing down of the ions around z = -16 mm for r = 13 mm is due to the fact that Fig. 7 depicts the most probable velocity, hence the main peak. In this region, the VDF is composed of two major peaks and one becomes predominant over the other, due to the complexity and irregularity of the ionization region. The electric field is determined using the most probable velocity as well, overlooking ionization effects and departure from a Maxwellian VDF, which are the reasons for its reversal.

3.2 Radial evolution of lineshape

As represented in Fig. 1, the lineshape of the ion transition was measured at seven different radial locations for z = -14 mm. The measured data can be viewed in Fig. 8. The main peak of the VDF has roughly the same velocity for any radius smaller than $\approx$ 9 mm, which suggests that the axial ion acceleration is quite uniform along the radial direction in the upstream half of the discharge chamber. This uniformity is altered close to the wall. In addition, the broadening of the VDF seems to confirm the overlap of the ionization and acceleration regions, at least in the 2 mm near the side wall.

4. Atoms axial velocity

4.1 Axial evolution of lineshape

In a similar way as for the ions, the xenon atoms were probed but in their resonant state $6s^2[3/2]_1^\circ$, along the axial direction. The measurements were done right at the exit of one injector hole, at z = -22 mm, to ensure collecting signal, and scans were done at several axial locations up to z = -14 mm, where the signal-to-noise ratio became too small. The results are given in Fig. 9a. The important Zeeman splitting causes the spectra to depart from the actual atom VDF, but the peaks are not displaced along z which shows that the neutral gas is not accelerated along the axial direction. The minor broadening shows that there is some, but little heating, which confirms the previous conclusions about the ion apparent heating (VDF broadening) being due to the creation of ions within the acceleration region. The neutral heating is a thermal effect in the order of a few hundred Kelvin while the ion heating is mainly a kinetic effect in the order of 10000 K. Given that the spectra do not give information on the VDF straight away, these conclusions about the neutral velocity and temperature are confirmed by modeling the lineshapes, which is described in greater detail in

(a) Along the axial direction, r = 13 mm

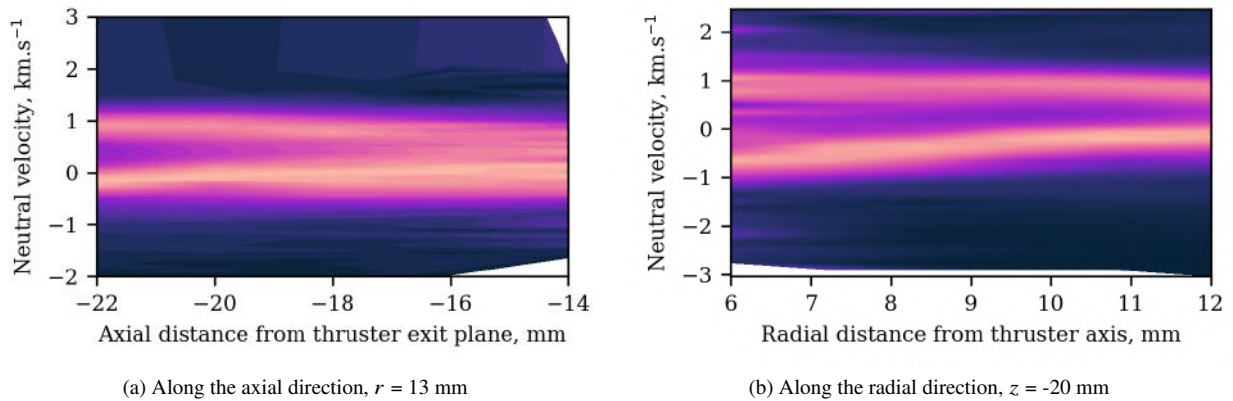(b) Along the radial direction, z = -20 mm

Figure 9: Evolution of the xenon atoms transition lineshape.

Section 5.2. The poor signal a few millimeters downstream of the injector is attributed to the lack of sufficiently hot electrons to generate excitation collisions with the neutrals, in addition to the expected decreasing neutral density that naturally reduces collision frequencies.

On the left-hand side of Fig. 9a, one can see the effect of Zeeman splitting more clearly than in the ions spectra, since the neutrals are cold and closer to a monoenergetic population, so any splitting is not hidden by other broadening mechanisms.

The resonant transition $6s^2[3/2]_2^\circ \to 6p^2[3/2]_2$, with an excitation and fluorescence wavelength of 823.16336 nm, was also probed in an attempt at collecting more signal. It was successful since it allowed for getting spectra as far downstream as z = -8 mm but these data are not shown given the complexity of the lineshape and the difficulty of extracting useful information from it. However, the presence of signal further downstream with this transition confirms the hypothesis that atoms are difficult to detect because electrons do not sufficiently bring them to excited states in this plasma, but a neutral population is still present.

4.2 Radial evolution of lineshape

The evolution of the neutrals lineshape along the radial direction at z = -20 mm is represented in Fig. 9b. The signal is shifted towards velocities ≈ 100 m.s^{-1} larger when approaching the side wall. Although this behavior cannot be interpreted right away as a change of velocity since the raw lineshape is not directly representative of the VDF in the conditions of measurement, spectra models confirmed this minor change of velocity. However, since Fig. 9b represents the variation in the radial direction, it is possible that a slight decrease in axial velocity closer to the thruster axis is only due to the velocity vector becoming less axial and partially radial, away from the injector hole.

In addition, the lineshape gets narrower at larger radii, which is due to the magnetic flux decreasing as r increases, thus increasing the Zeeman splitting. This was also confirmed by spectra simulations, as presented in Section 5, since it is not straightforward to isolate from other effects such as the temperature of the neutrals.

Like for the scans presented in Section 4.1, the signal-to-noise ratio becomes very poor a few millimeters away from the injector, as r decreases.

5. Spectra simulations

5.1 Model introduction

As introduced in Section 2.3.1, there exist many mechanisms that concurrently contribute to broadening and splitting the fluorescence lineshape. In some cases, the spectrum is so complex that it does not maintain the shape of the VDF of the probed species and the use of a theoretical model becomes necessary to retrieve the real distribution function, while accounting for all these effects. The model used in this work was developed by Vinci, and a more thorough description of it can be found elsewhere.[5, 13, 22] The principle of the model consists of applying selection rules to determine all the optical transitions allowed in the absorption process and finding the intensity and energy shift of each of them. Phenomena represented by the model include the isotopic shift, the hyperfine structure, and magnetic field effects such as Zeeman and Paschen-Back. An initial VDF shape, combining one or two Gaussian distributions, is assumed and

9

(a) Xe II, r = 0 mm, z = -22 mm

(b) Xe II, r = 0 mm, z = -12 mm

(c) Xe II, r = 13 mm, z = -8 mm

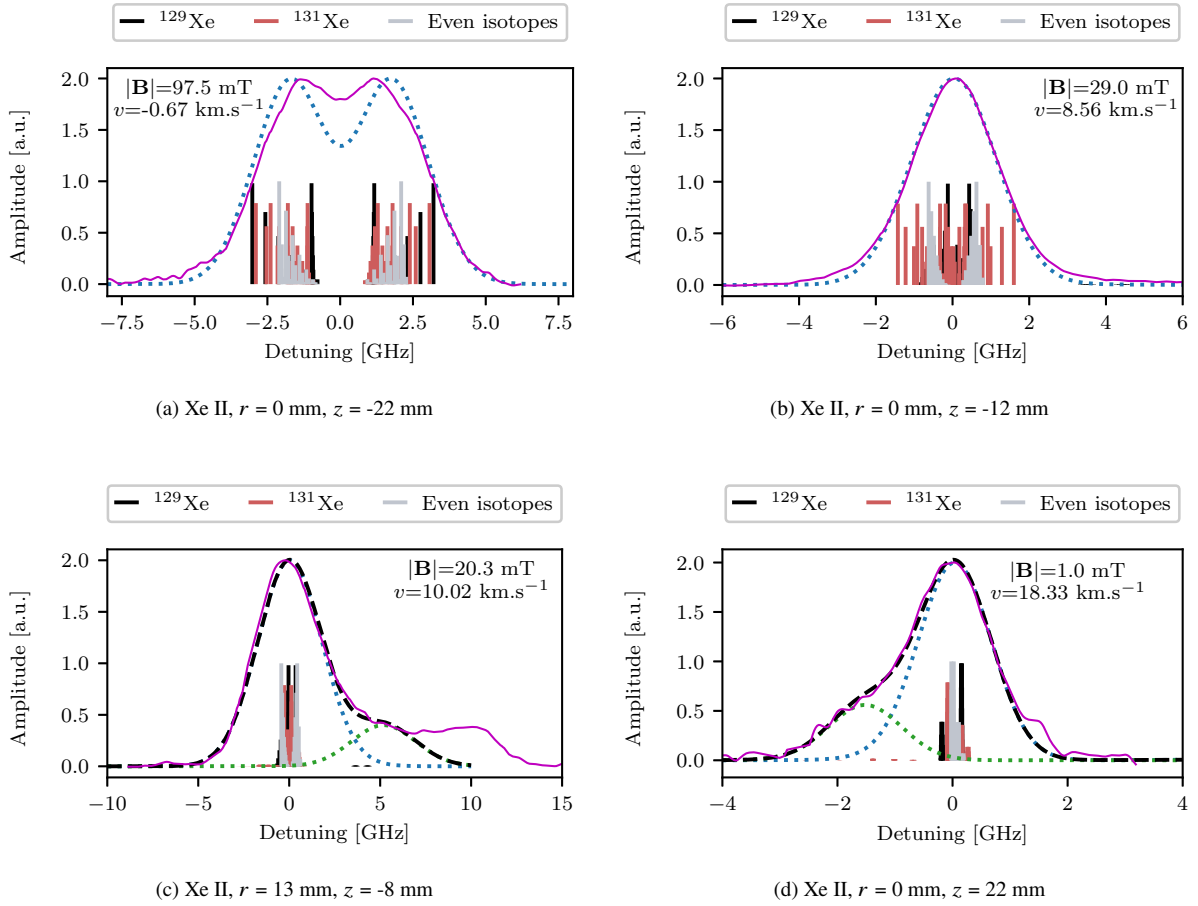(d) Xe II, r = 0 mm, z = 22 mm

Figure 10: Experimental (solid magenta) and modeled transition lineshapes for xenon ions at different axial positions. The dotted blue line shows the reconstructed lineshape of the main population. When two populations are modeled, the dotted green line shows the reconstructed lineshape of the second population and the dashed black line shows the full reconstructed spectrum.

the lineshape is retrieved by fitting the experimental spectrum to the computed one, which allows for estimating the Doppler shift. The model takes as input the measured fluorescence profile, the local magnetic field, and the probed species and optical transition.

There are uncertainties and assumptions limiting the fidelity of the model but it has demonstrated great capability of rebuilding experimental lineshapes measured in various plasma thrusters. Note that, in this work, the laser beam is assumed strictly σ-polarized, but in practice, various uncertainties in the experimental setup (error in the angle of polarization of the laser, errors in the alignment of the laser and the thruster, misalignment of the coil and the discharge chamber, etc.) could mean there is a non-zero component of the laser polarization angle in the direction parallel to the magnetic field, thus introducing the possibility of π transitions occurring.[23]

5.2 Spectra simulation results analysis

The fluorescence lineshapes obtained experimentally and presented in Sections 3 and 4 have been simulated with the model to clearly identify the spectra that presented broadening and the ones with peculiar non-Gaussian VDFs. In all the figures of Section 5.2, the smoothed experimental lineshape is shown as a solid magenta line, the modeled optical transitions are shown with vertical bars, the reconstructed lineshape of the main population is shown as a dotted blue line. Each population lineshape is rebuilt assuming it has a Doppler-shifted Gaussian distribution. The spreading of the distribution, hereafter also termed *temperature*, is a parameter varied to fit the modeled lineshape to the measured data. Whenever two Gaussians are used, they have equal velocity dispersion and the difference in Doppler shift between them is a fixed parameter given as input, as well as the ratio of their densities.

Figure 10 presents the simulated metastable ion spectra at four measurement locations. Figure 10a shows the lineshape

(a) Xe I, r = 13 mm, z = -22 mm
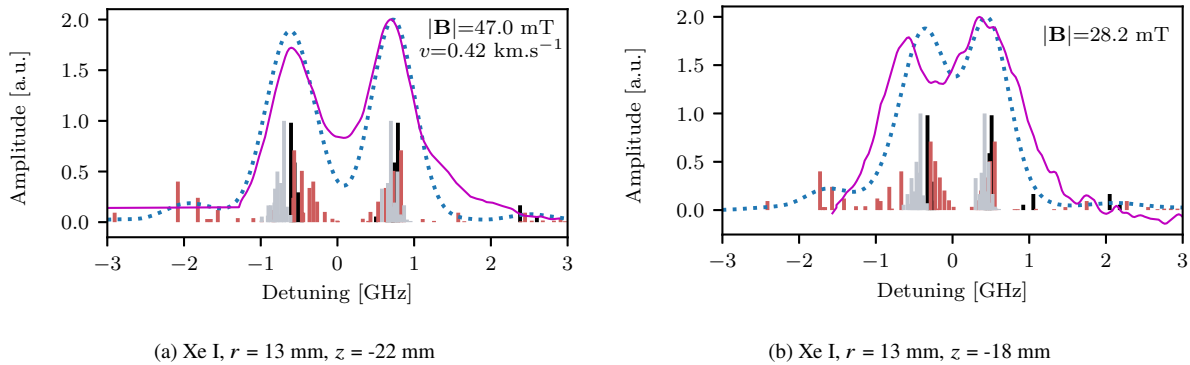

(b) Xe I, r = 13 mm, z = -18 mm

Figure 11: Experimental (solid magenta) and modeled transition lineshapes for xenon atoms at different axial positions. The dotted blue line shows the reconstructed lineshape of the main population.

acquired at the point of strongest magnetic flux in the thruster chamber. The model demonstrates that the two wide peaks are due to Zeeman splitting, while the real ion VDF can reasonably be considered Gaussian. The dip between the two peaks is not as deep as the model predicts, which is attributed either to a slight underestimation of the magnetic flux or to alignment errors causing the occurrence of π transitions.[13] Modeling the line allows for determining without ambiguity the real Doppler shift of the ions in that region and confirms that their velocity is negative, and thus directed towards the central pole ceramic.

Figure 10b shows an example in which the raw lineshape reflects much better the actual ion VDF, besides some broadening with respect to the initial distribution.

In the case of Fig. 10c, the main peak can be reconstructed considering a population with a Gaussian distribution. However, the ions present at all the velocities from zero to the most probable one (as described in Section 3.1) cannot be simulated with this type of distribution. The model confirms that the peculiar lineshape near the side wall is representative of the VDF and is not caused by some broadening effect but by the presence of slow ions instead.

Finally, Fig. 10d shows a case far downstream on the axis, where the spectrum images well the ion VDF and contains a population of fast ions. The overall fluorescence lineshape is correctly evaluated as the sum of the signals from two groups with Gaussian distributions.

The xenon atom transition was also modeled and two spectra are shown in Fig. 11. The fluorescence signal measured at the closest point to the gas injector is provided in Fig. 11a. It displays very clear Zeeman splitting due to the relatively strong magnetic field in the probed region (470 G), and the fact their velocity dispersion is one order of magnitude smaller than the one of the ions. The reconstructed lineshape allows once again for demonstrating that the two peaks of the spectrum are not a feature of the neutral VDF, but rather of the complexity of the transition itself and the broadening mechanisms. The slight mismatch between the experimental and modeled curves is attributed mainly to potential alignment error and laser reflection in the copper anode.

Figure 11b shows the simulation of the neutral transition spectrum 4 mm downstream of the one in Fig. 11a. The signal-to-noise ratio is clearly poorer, but the model still grasps the general shape of it. The same double peak due to Zeeman effect is visible. The shift between the measurement and the model is attributed, in this case, to an underestimation of the magnetic flux at the probed point, and potential alignment error too. Modeling the lineshape while supposing $|\vec{B}|$ a few percent larger than the expected value allows for better matching of the two curves. Both plots in Fig. 11 are obtained by considering the same kinetic temperature of 800 K. The slightly broader lineshape in Fig. 11b causes poor matching of the model which suggests that the neutrals are a few hundred degrees hotter there, probably due to the collisions occurring in this region where the neutral and plasma densities are the highest.

Simulations like the ones depicted in Fig. 10 were performed for all the measured ion transition lineshapes and the kinetic temperature was estimated according to the procedure described herein above in Section 5.2. The results are given in Fig. 12, they correspond to the temperature from the standard deviation of the distribution fit for the main population. In some cases, the departure from a single or double Gaussian distribution does not allow for getting a good fit of the whole lineshape and only the main peak is considered.

The ion temperature varies very little on the axis with values below 1 eV. However, there is some very significant apparent heating inside the discharge chamber, over the first 4 mm on the quarter-line and over the first 12 mm near the side wall. As mentioned in Section 3, this is caused by the broadening of the ion VDF where the ionization and acceleration regions overlap. Simulations of the neutrals measurements (Fig. 11) showed no heating of the atoms besides a few hundred Kelvin over 8 mm near the side wall, which confirms that the apparent increase of ion velocity
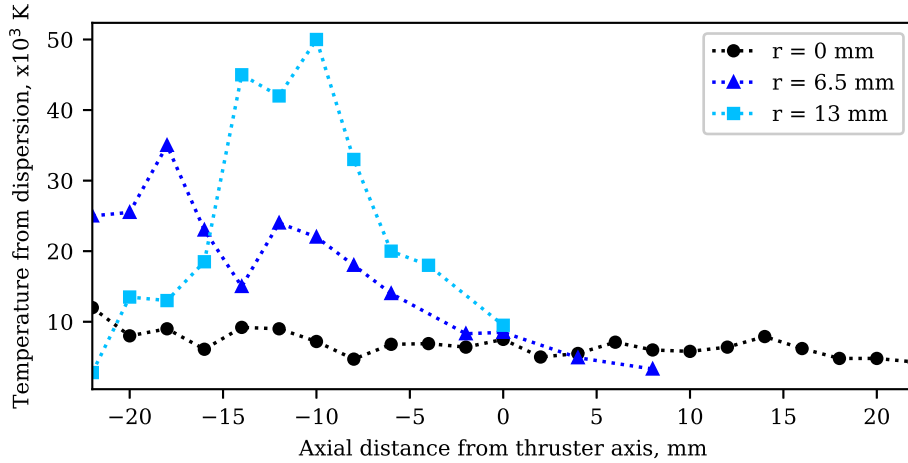
Figure 12: Variation along the axial direction, at three different radii, of the ion temperature obtained from the velocity spread of the Gaussian fitted with spectra simulations.

dispersion in that region is a kinetic effect rather than a thermal one.

For r = 6.5 mm and r = 13 mm, the ions appear to cool down as they move toward the plume. The fact that the inflection of the temperature trend occurs further downstream as r increases is likely due to the magnetic topology and the location of the injector at r = 12 mm, creating an ionization region roughly bound between the anode, the side wall, and a magnetic streamline intersecting both walls. The apparent cooling downstream of this region is unexpected since the dispersion in kinetic energy should be preserved. However, it could be due to the acceleration of slow ions toward large angles, thus decreasing the intensity of their signal as z increases, compared to the fluorescence of the fastest and most axial ions. This behavior would be consistent with previous observations on the Ion Energy Distribution Function measured with a Retarding Potential Analyzer in the same device.[20]

6. Conclusions

This work presented the results of the measurement of the axial Velocity Distribution Function of xenon ions and atoms in the discharge chamber and near-field of a 200 W Cylindrical Hall Thruster. The characterization was done by means of Laser-Induced Fluorescence spectroscopy since it is a non-intrusive diagnostic that provides information on the species velocity with high accuracy and spatial resolution. The principle of this method relies on the Doppler shift of the absorbed laser light, and the detection of the intensity of the emitted fluorescence light.

Various axial and radial locations were probed to assess the behavior of the two species and their interaction with the thruster walls and the applied magnetic field, which is one of the main differences between traditional and cylindrical HETs. These measurements allowed for identifying the location of the peak axial electric field at three different radii, which was unexpectedly found at very similar axial positions in all cases. Obtaining an image of the full ion VDF and its evolution in the probed plane demonstrated an overlap between the ionization and acceleration region at all radii inside the discharge chamber, resulting in a non-Maxwellian VDF. In particular, it was observed that ions are created all along the side wall, they are visible in the slow part of the VDF. Ions traveling on the axis toward the central pole were observed as well.

Given the multiple broadening and splitting effects altering the fidelity of the lineshape to the actual VDF, and more specifically the strong magnetic field characteristic of the CHT, the measured spectra were reconstructed using an existing theoretical model. This allowed for discriminating actual features of the VDF from other effects. It provided information such as the occurrence of thermal heating of the xenon atoms moving toward the plume, and the kinetic heating of the ions within the thruster chamber. The hypothesis is made that slow ions are being accelerated to larger angles due to the topology and magnitude of the electric field that varies over the ionization region, resulting in the slow population not showing in the VDF on the axis, far in the plume.

The results presented herein above provide useful insight into the dynamics of the plasma discharge inside the CHT and in the near plume. They highlight some particularities of this geometry in comparison with traditional annular Hall thrusters, and suggest possible design improvements. Among those, moving the injection away from the side wall could mitigate the ion flux to the side wall and possible recombination and re-ionization. The channel length could certainly be reduced since most of the acceleration occurs before the exit plane. This test campaign also confirmed that

the erosion of the central pole is one of the main issues in a CHT. Even though LIF spectroscopy is a powerful tool to understand the behavior of heavy particles in the thruster, the need for lineshape modeling capabilities to retrieve their actual VDFs appeared evident. Further work on the use of spectra simulations is required to clarify any mismatch between the model and the experiments. Finally, it could be of great interest to characterize the velocity distribution and the electric field in two dimensions with an adapted LIF setup, particularly with the magnetic topology and the global design features of this CHT.

7. Acknowledgments

References

[1] Y. Raitses, L. A. Dorf, A. A. Litvak, and N. J. Fisch. Plume reduction in segmented electrode Hall thruster. *Journal of Applied Physics*, 88(3):1263–1270, August 2000.

[2] Stéphane Mazouffre. Laser-induced fluorescence spectroscopy applied to electric thrusters.

[3] S Mazouffre, G Bourgeois, K Dannenmayer, and A Lejeune. Ionization and acceleration processes in a small, variable channel width, permanent-magnet Hall thruster. *Journal of Physics D: Applied Physics*, 45(18):185203, May 2012.

[4] Alfio E. Vinci, Quentin Delavière–Delion, and Stéphane Mazouffre. Electron thermodynamics along magnetic nozzle lines in a helicon plasma. *Journal of Electric Propulsion*, 1(1):4, December 2022.

[5] Alfio E Vinci, Marco R Inchingolo, Stéphane Mazouffre, and Jaume Navarro-Cavallé. Ion dynamics in the magnetic nozzle of a waveguide ECR thruster via laser-induced fluorescence spectroscopy. *Journal of Physics D: Applied Physics*, 56(2):025204, January 2023.

[6] Christoph Eichhorn, Lukas Pietzonka, Frank Scholze, Carsten Bundesmann, Daniel Spemann, Horst Neumann, and Hans J. Leiter. Single- and two-photon absorption laser-induced fluorescence spectroscopy in rare gases for gridded ion thruster diagnostics. *EPJ Techniques and Instrumentation*, 9(1):2, December 2022.

[7] Clemence Royer, Alfio E. Vinci, Stephane Mazouffre, Thibault Hallouin, and Antonio Gurciullo. A LIF study on the plasma plume of a cluster of two 100 W Hall thrusters. In *37th International Electric Propulsion Conference Massachusetts Institute of Technology, Cambridge, MA, USA*, 2022.

[8] Y. Dancheva, V. Biancalana, D. Pagano, and F. Scortecci. Measurement of XeI and XeII velocity in the near exit plane of a low-power Hall effect thruster by light induced fluorescence spectroscopy. *Review of Scientific Instruments*, 84(6):065113, June 2013.

[9] Vernon H. Chaplin, Ryan W. Conversano, Alejandro Lopez Ortega, Ioannis G. Mikellides, Robert B. Lobbia, and Richard R. Hofer. Ion Velocity Measurements in the Magnetically Shielded Miniature (MaSMi) Hall Thruster Using Laser-Induced Fluorescence. In *6th International Electric Propulsion Conference, University of Vienna, Austria*, 2019.

[10] Guentae Doh, Holak Kim, Dongho Lee, Sanghoo Park, Stéphane Mazouffre, and Wonho Choe. Structure of the ion acceleration region in cylindrical Hall thruster plasmas. *Journal of Physics D: Applied Physics*, 55(22):225204, June 2022.

[11] Spektor. LIF Measurements of the Cylindrical Hall Thruster Plume. 2009.

[12] Natalia A MacDonald, Mark A Cappelli, and William A Hargus. Laser-Induced Fluorescence Velocity Measurements of a Low Power Cylindrical Hall Thruster.

[13] Alfio E. Vinci, Stéphane Mazouffre, Marco R. Inchingolo, Victor Gomez, Pablo Fajardo, and Jaume Navarro-Cavallé. Probing xenon atoms and ions velocity in the magnetic nozzle of a helicon plasma thruster. In *37th International Electric Propulsion Conference*, Massachusetts Institute of Technology, Cambridge, MA, USA, 2022.

[14] Artem Smirnov, Yegeny Raitses, and Nathaniel J. Fisch. Experimental and theoretical studies of cylindrical Hall thrusters. *Physics of Plasmas*, 14(5):057106, 2006.

[15] Yevgeny Raitses, Enrique Merino, and Nathaniel J Fisch. Cylindrical Hall thrusters with permanent magnets. *Journal of Applied Physics*, page 10, 2010.

[16] Yuanyuan Gao, Hui Liu, Peng Hu, Hongyan Huang, and Daren Yu. The effect of magnetic field near the anode on cylindrical Hall thruster. *Plasma Sources Science and Technology*, 25(3):035011, June 2016.

[17] Yevgeny Raitses, Artem Smirnov, Erik Granstedt, and Nathaniel Fisch. Optimization of Cylindrical Hall Thrusters. In *43rd AIAA/ASME/SAE/ASEE Joint Propulsion Conference & Exhibit*, Cincinnati, OH, July 2007. American Institute of Aeronautics and Astronautics.

[18] Holak Kim, Wonho Choe, Youbong Lim, Seunghun Lee, and Sanghoo Park. Magnetic field configurations on thruster performance in accordance with ion beam characteristics in cylindrical Hall thruster plasmas. *Applied Physics Letters*, 110(11):114101, March 2017.

[19] Tatiana Perrotin, Adrián Domínguez-Vázquez, Jaume Navarro-Cavallé, Pablo Fajardo, and Eduardo Ahedo. Design and Preliminary Study of a 200W Cylindrical Hall Thruster. In *Space Propulsion Conference*, page 11, Estoril, Portugal, 2021.

[20] Tatiana Perrotin, Alfio E. Vinci, Stéphane Mazouffre, Jaume Navarro-Cavallé, Pablo Fajardo, and Eduardo Ahedo. Characterization of a low-power Cylindrical Hall Thruster. In *37th International Electric Propulsion Conference*, Massachusetts Institute of Technology, Cambridge, MA, USA, June 2022.

[21] Garrigues, Santhosh, Grimaud, and Mazouffre. Operation of a low power Hall thruster with a shielded magnetically configuration. In *36th International Electric Propulsion Conference*, University of Vienna • Vienna, Austria, 2019.

[22] Alfio E Vinci, Stéphane Mazouffre, Víctor Gómez, Pablo Fajardo, and Jaume Navarro-Cavallé. Laser-induced fluorescence spectroscopy on xenon atoms and ions in the magnetic nozzle of a helicon plasma thruster. *Plasma Sources Science and Technology*, 31(9):095007, September 2022.

[23] Wensheng Huang, Timothy Smith, and Alec Gallimore. Obtaining Velocity Distribution Using a Xenon Ion Line with Unknown Hyperfine Constants. In *40th AIAA Plasmadynamics and Lasers Conference*, San Antonio, Texas, June 2009. American Institute of Aeronautics and Astronautics.

[24] Thibault Hallouin and Stéphane Mazouffre. Far-Field Plume Characterization of a 100-W Class Hall Thruster. *Aerospace*, 7(5):58, May 2020.

[25] Atsushi Shirasaki and Hirokazu Tahara. Operational characteristics and plasma measurements in cylindrical Hall thrusters. *Journal of Applied Physics*, 101(7):073307, April 2007.